Design and Control of Inductive Power Transfer System for Electric Vehicles Considering Wide Variation of Output Voltage and Coupling Coefficient

Minkook Kim, *Student Member, IEEE*, Dong-Myoung Joo, *Student Member, IEEE*,
and Byoung Kuk Lee, *Senior Member, IEEE*

***Abstract*—In this paper, a design and control scheme of the inductive power transfer (IPT) system for electric vehicles are proposed, considering a wide variation in output voltage and coupling coefficient. The characteristics of the proposed IPT system and a design method for the resonant network are suggested. By utilizing the battery management converter at the secondary side, the design and control can be simplified while managing the output voltage and power of the battery. In order to achieve high efficiency by reducing the voltage–ampere rating, zero phase angle tracking control is proposed. In addition, a phase-shift control is applied to the primary side to ensure the stable system operation by limiting output voltage. A 3.3-kW laboratory prototype with magnetic power pads is manufactured, and the validity of the proposed design and control is verified through experimental results using the laboratory prototype.**

***Index Terms*—Battery management (BM) converter, coupling coefficient, inductive power transfer (IPT), wireless power transfer (WPT), zero phase angle operation.**

I. INTRODUCTION

INDUCTIVE power transfer (IPT) systems, which are a type of wireless power transfer (WPT) technology, are recently experiencing fast development and an increasing demand in many applications, such as portable appliances and electric vehicle (EV) chargers. Because of its physically separated configuration, the IPT system can provide several advantages to both vehicle manufacturers and end users. For designers and manufacturers, its inherent galvanic isolation and robustness to humid, volatile, or dusty environments can reduce the complexity of the EV design. For end users, safety and comfort can be improved, as they do not need to provide additional work to initiate EV charging. In order to improve the above-mentioned advantages and spread them to the industry and end users, research on the IPT system has been actively performed. The

Manuscript received November 2, 2017; revised January 1, 2018 and March 21, 2018; accepted April 26, 2018. Date of publication May 9, 2018; date of current version December 7, 2018. Recommended for publication by Associate Editor J. Acero. *(Corresponding author: Byoung Kuk Lee.)*

The authors are with the Department of Electrical and Computer Engineering, Sungkyunkwan University, Suwon 16419, South Korea (e-mail:

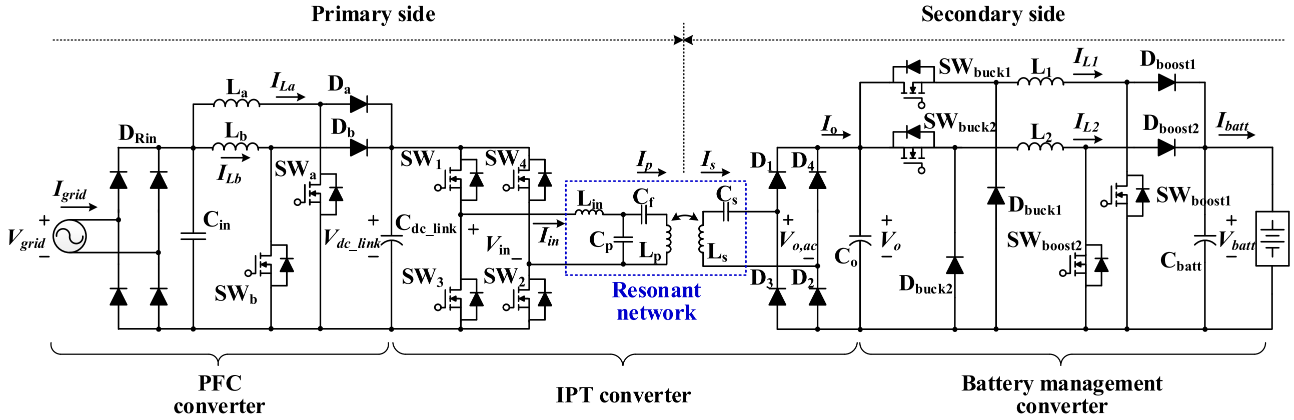

Fig. 1. Schematic of the proposed IPT system.

and battery voltage within a designated operating frequency. By adopting a compensation network with load-independent current characteristics and frequency control, CC-CV charging profile is implemented [20], [21]. However, in [20], coupling variation is not considered and the operating frequency range is relatively wide to meet interoperability of the IPT system [19]. In [21], both coupling and battery voltage variations are considered while implementing the CC-CV charging profile. However, additional intermediate coils make the IPT system bulky and the secondary magnetic power pad, which is identical the size as the primary side, is too large and heavy to be attached to the bottom of the EVs.

In this paper, a design and control of the IPT system that can counteract fluctuations of coupling coefficient and battery voltage are proposed. By adopting the battery management (BM) converter, which is a cascaded buck–boost converter, at the secondary side of the IPT system, the CC-constant power (CP) CV battery charging profile is easily implemented. Further, a design process of the resonant network is presented and control algorithms for the ZPA operation and phase shift control for output voltage limitation, while satisfying the operating frequency range of the standard, are suggested. Utilizing the proposed ZPA tracking control, the IPT converter can be operated within a narrow operating frequency variation range. The validity of the proposed design and the control method is verified using the 3.3-kW laboratory prototype with manufactured magnetic power pads.

II. DESIGN OF AN IPT SYSTEM

A. Power Conversion System

An IPT system comprises two magnetically coupled electrical systems. In terms of power conversion system (PCS), the proposed system is classified into three stages: power factor correction (PFC) converter, IPT converter, and a cascade buck–boost dc–dc converter (BM converter). The schematic of the proposed IPT system is shown in Fig. 1.

In order to meet the IEEE-519 standard, which deals with the harmonic measurements and recommend harmonic limits for voltage and current distortion, a boost PFC converter with an analog controller (UCC28070) is used at the first stage of the proposed system [22]. The IPT converter is composed of a full-bridge inverter; resonant network, which includes primary, secondary power pads and compensation capacitors; and diode rectifier. For the purpose of corresponding input and output voltage variations caused by coupling fluctuation and SOC of the battery, a BM converter is adopted at the final stage of the system. For digitally controlling the IPT and BM converters, the microcontroller TMS320F28335 of Texas Instruments is utilized. The PFC and BM converters are a two-phase design to retain redundancy and achieve high performance.

TABLE I
ELECTRICAL SPECIFICATION OF THE IPT SYSTEM

Parameter	Value	
V_{grid}	220	$\mathrm{V_{rms}}$
V_{dc_link}	380	$\mathrm{V_{dc}}$
V_o	165–450	$\mathrm{V_{dc}}$
V_{batt}	240–410	$\mathrm{V_{dc}}$
P_{batt}	3.3	kW
f_o	85	kHz
f_{sw}	81.38–90	kHz
k	0.062–0.202	

Since the coupling coefficient k of the IPT system is greatly influenced by the parking position of the EVs, considerations of the vertical gap and horizontal misalignment of EVs are necessary to deliver the desired power to the battery. In this paper, both the Z_1 (55–105 mm) and Z_2 (95–165 mm) classes are considered for system design and control. Thus, the vertical gap is set to 55–165 mm and the horizontal misalignment for the x- and y-axis is ±75 mm, which results in a difference of approximately three times k. In general, Li-ion batteries are commonly used for the high-voltage battery pack of the EVs. The nominal voltage of the Li-ion battery cell is 3.7 V, and its voltage range should be managed from 3.2 to 4.2 V to protect against deterioration or explosion of the batteries. In this paper, the charging voltage range of the battery pack is selected as 240–410 V, 100 cells connected in series, to satisfy the stable charge and voltage drop condition caused by over discharge of the batteries. Table I shows the electrical specification of the proposed system.

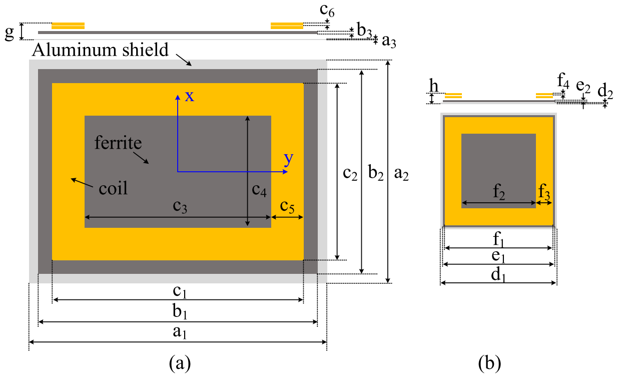

Fig. 2. Configuration of the magnetic power pads. (a) Primary pad. (b) Secondary pad.

B. Magnetic Power Pads

Because of the loosely coupled characteristic of the IPT system, k of the magnetic power pads in the IPT system is low, and its range is effectively 0.1–0.3. The system performance of the IPT system is a function of k and the coil quality factor Q of the IPT coils and it is defined as figure of merit [6]. In order to achieve high efficiency in the loosely coupled system, high k and Q are desirable. Thus, a variety of studies on the magnetic power pads have been performed, and their characteristics and performance have been compared [23]–[27]. The circular pad (CP) is one of the most common coil structures, and its coupling drastically decreases as the misalignment increases to either the x- or y-axis. The double-D pad (DDP) is developed to improve the coupling performance at misalignment conditions. The double-D and quadrature pad and the bipolar pad are developed to combine the advantages of the CP and the DDP. Unlike k depends on the configuration and relative position of the magnetic power pads, Q is affected by the loss of the magnetic power pads. There have been many attempts to analyze the loss of the magnetic components numerically but the finite element method (FEM) simulation is utilized due to its nonlinear characteristics [28], [29].

The rectangular and square structures are adopted for the primary and secondary power pads, respectively [19]. A double-layer coil structure is adopted for both power pads to acquire inductance. The structure of the ferrite is decided by flat plate for coupling enhancement, reluctance reduction, and flux guidance, whereas the aluminum shield is utilized to mitigate the effect of the leakage flux. Fig. 2 illustrates the configuration of the magnetic power pads, and indications of the x- and y-axis are also presented and the detailed values are summarized in Table II. After determining the configuration and dimensions of the magnetic power pads, the maximum inductances of the primary and secondary power pads should be estimated using FEM simulation. This procedure is necessary to reduce the trial and error iterations for coil turn number determination by setting the implementable maximum coil inductances. In this design, maximum inductances for the primary and the secondary coils are approximately 1000 and 300 μH, where the number of maximum turns for each coil is 26 and 30, respectively.

TABLE II
DIMENSIONS AND PARAMETER INDICATIONS OF THE POWER PADS

	Value [mm]		Value [mm]	Parameter indication	
a_1	640	c_6	5.5	$a_{1\text{-}3}$	Primary aluminum shield
a_2	480	d_1	250	$b_{1\text{-}3}$	Primary ferrite
a_3	2	d_2	3	$c_{1\text{-}6}$	Primary coil
b_1	600	e_1	242	$d_{1,2}$	Secondary aluminum shield
b_2	440	e_2	4	$e_{1,2}$	Secondary ferrite
b_3	6	f_1	232	$f_{1\text{-}4}$	Secondary coil
c_1	540	f_2	160	g	Primary pad total height
c_2	380	f_3	36	h	Secondary pad total height
c_3	400	f_4	2.5		
c_4	240	g	35.3		
c_5	70	h	23		

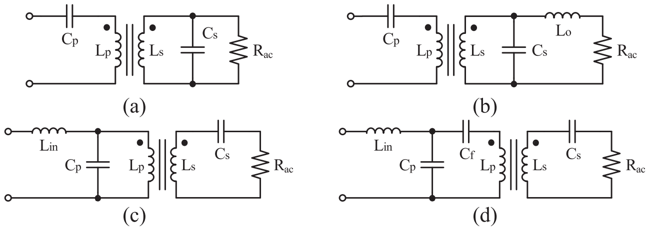

Fig. 3. Circuit diagram of the resonant network. (a) SP topology. (b) S-*LCL*. (c) *LCL*-S. (d) *LCCL*-S.

III. DESIGN OF A RESONANT NETWORK

A. Characteristics of the Resonant Network

The battery voltage of the conventional research is fixed for analysis simplification [6]. In the proposed system, the BM converter controls the battery voltage and power considering the wide variation of the battery voltage and coupling coefficient. In order to simply control the system, a constant output voltage V_o of the IPT converter is desirable. Among various types of resonant networks with constant output voltage characteristics, SP, S-*LCL*, *LCL*-S, and *LCCL*-S are considered. Fig. 3 illustrates the circuit diagram of the resonant networks. The notation S represents the series-connected capacitors, and P represents the parallel-connected capacitors. In the case of the SP and S-*LCL* topologies, the voltage stress of the secondary compensation capacitor C_s and primary resonant current I_p are small, whereas the voltage stress of the primary compensation capacitor C_p and secondary resonant current I_s are large. Additionally, due to the characteristic that V_o increases as k decreases, a low limit for k is necessary when utilizing SP or S-*LCL* topologies for the resonant network in the IPT system. Further, the bifurcation phenomena, which is affected by coupling or load condition, may occur at high k or light loads [31]. Contrary to the SP and S-*LCL* topologies, the primary current of the *LCL*-S topology is constant regardless of k, and the load and induced voltage on the secondary side is also constant

$$V_s = j\omega M I_p. \tag{1}$$

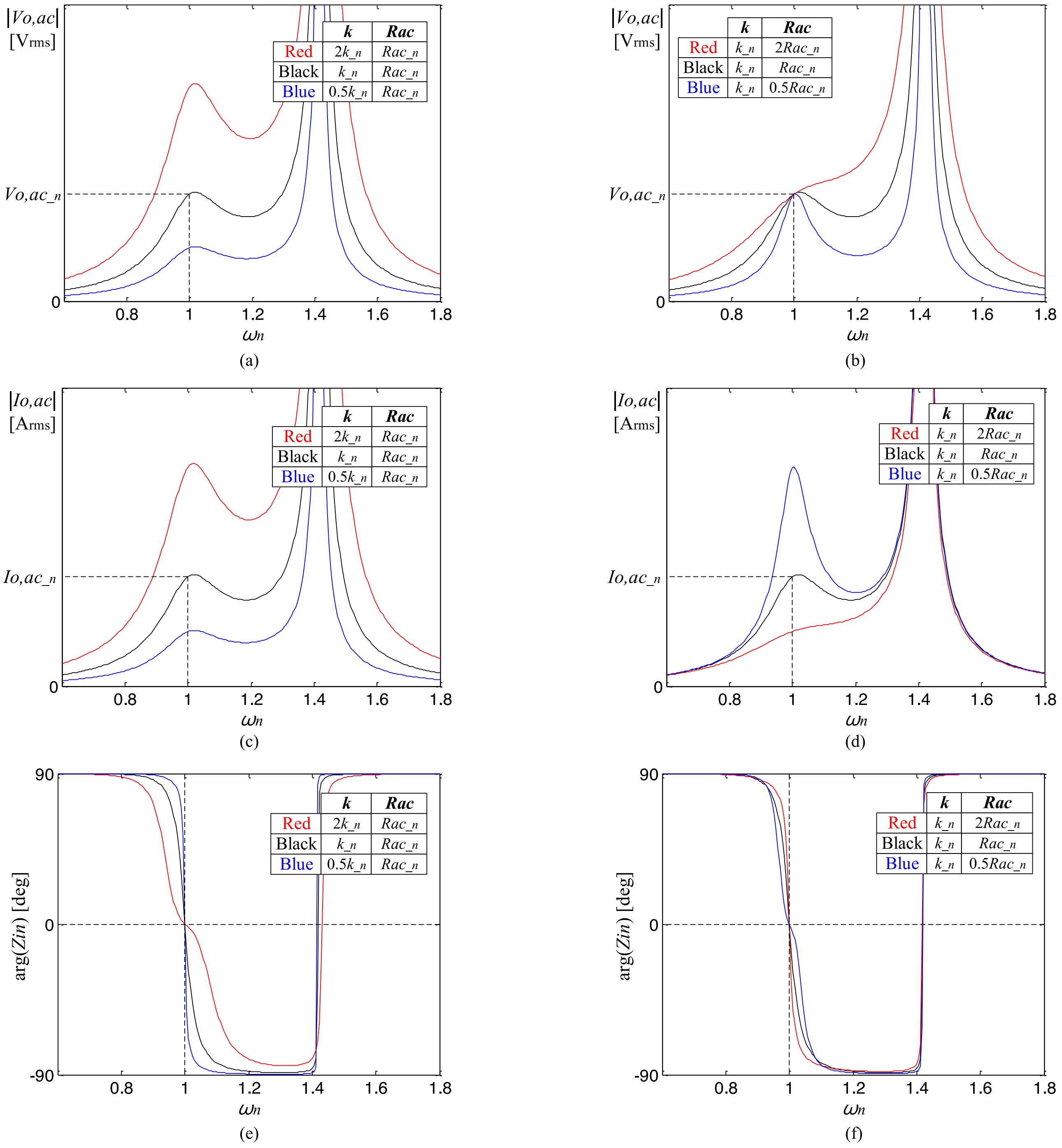

(a)

(b)

(c)

(d)

(e)

(f)

Fig. 4. Output characteristic and impedance curves of the *LCCL*-S topology. (a) $|V_{o,\mathrm{ac}}|$ with k variation. (b) $|V_{o,\mathrm{ac}}|$ with R_{ac} variation. (c) $|I_{o,\mathrm{ac}}|$ with k variation. (d) $|I_{o,\mathrm{ac}}|$ with R_{ac} variation. (e) Arg(Z_{in}) with k variation. (f) Arg(Z_{in}) with R_{ac} variation.

In addition, not only the voltage stresses of C_p and I_s are relatively small but also the possibility of bifurcation is low because of C_p [31]. In case of the *LCL*-type topologies, the values of the input inductance L_{in} and primary inductance L_p should be identical and resonate with C_p at the resonant frequency. However, if the values of L_{in} and L_p are too large or too small, an implementation of the system is difficult. Especially, when their inductances are small, an intensively large I_p lowers the system efficiency. Thus, in order to understand the limitation of the *LCL*-S topology, *LCCL*-S topology is adopted. By adding the filter capacitor C_f in series with L_p, the impedance increase in the primary power pad can be alleviated. A series-connected C_f can also eliminate the dc offset of I_p, which results in solving the high current stress at the transient state. The output voltage of the *LCCL*-S topology is constant regardless of the load at fixed k condition. Fig. 4 shows the output characteristics and

TABLE III
DESIGNED PARAMETERS OF THE RESONANT NETWORK

Parameter	Value	
L_p	399	μH
L_s	170	μH
L_{in}	37.19	μH
C_p	94.271	nF
C_f	9.689	nF
C_s	20.623	nF
V_{in}	342.15	$\mathrm{V_{rms}}$
V_o	165	$\mathrm{V_{dc}}$
P_o	3350	W
f_o	85	kHz
k	0.062	

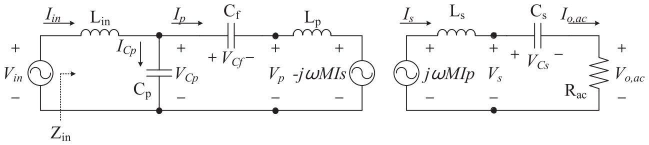

Fig. 5. Equivalent circuit of the *LCCL*-S resonant network.

impedance of the *LCCL*-S topology. The parameters in Table III are utilized for the simulation and *k_n* is normalized coupling coefficient and R_{ac_n} can be calculated using P_o and V_o.

B. LCCL-S Resonant Network

In order to design an *LCCL*-S resonant network, six passive components, $L_p, L_s, C_s, L_{\text{in}}$, and C_p, and C_f, V_o, output power P_o, and k should be determined. Because the design of the resonant network is based on the fundamental harmonic analysis (FHA), the fundamental components of the voltage and current are considered. The equivalent circuit of the *LCCL*-S resonant network is shown in Fig. 5. R_{ac} represents the ac equivalent load resistance [32].

If the configuration of the coil, ferrite, and aluminum are decided, L_p and L_s are only dependent on the number of coil turn, so even if L_p and L_s are determined, the other four parameters can be numerically calculated to make the imaginary term of the input impedance Z_{in} zero [30]. C_s is calculated by

$$C_S = \frac{1}{\omega_0^2 L_S}. \tag{2}$$

L_{in} is designed considering the output power rating

$$L_{\text{in}} = kV_{\text{in}}\sqrt{\frac{L_P L_S}{R_{\text{ac}} P}}. \tag{3}$$

C_p is calculated to resonate with L_{in}

$$\omega_0 = \frac{1}{\sqrt{L_{\text{in}} C_P}} = \frac{1}{\sqrt{L_S C_S}}. \tag{4}$$

C_f should be designed to make the impedance of L_{in} and combined impedance of L_p and C_f identical

$$C_f = \frac{L_{\text{in}} C_P}{L_P - L_{\text{in}}} \quad \left(\because j\omega_0 L_{\text{in}} = j\omega_0 L_P + \frac{1}{j\omega_0 C_f}\right). \tag{5}$$

As previously stated, the coupling varies according to the parking position of the EVs, and V_o of the IPT converter is proportional to *k*. The design point is selected at a minimum coupling point ($k = 0.062$, vertical gap is 165 mm, and horizontal misalignment for the *x*- and *y*-axis is 75 mm), considering the stresses on the passive components and power semiconductors. Equations (6)–(15) show the formulas to calculate the voltage and current stresses of the primary and secondary sides

$$I_{\text{in}} = \frac{V_{\text{in}}}{Z_{\text{in}}} = \left(\frac{M}{L_{\text{in}}}\right)^2 \frac{V_{\text{in}}}{R_{\text{ac}}} \tag{6}$$

$$I_p = \frac{V_{\text{in}} - (-j\omega M I_s)}{Z_{p2}} + \frac{j\omega M I_s}{Z_{p3}} = -j\frac{V_{\text{in}}}{\omega_o L_{\text{in}}} \tag{7}$$

$$I_{Cp} = I_{\text{in}} - I_p = \left(\frac{M}{L_{\text{in}}}\right)^2 \frac{V_{\text{in}}}{R_{\text{ac}}} + j\frac{V_{\text{in}}}{\omega_o L_{\text{in}}} \tag{8}$$

$$I_s = I_{o,\text{ac}} = \frac{j\omega M I_p}{Z_{22}} = \frac{M V_{\text{in}}}{R_{\text{ac}} L_{\text{in}}} \tag{9}$$

$$V_{Cp} = V_{\text{in}} - j\omega L_{\text{in}} I_{\text{in}} = V_{\text{in}} - j\frac{\omega_o M^2 V_{\text{in}}}{R_{\text{ac}} L_{\text{in}}} \tag{10}$$

$$V_{Cf} = \frac{1}{j\omega C_f} I_p = \left(1 - \frac{L_p}{L_{\text{in}}}\right) V_{\text{in}} \tag{11}$$

$$V_p = j\omega L_p I_p - j\omega M I_s = \frac{L_p}{L_{\text{in}}} V_{\text{in}} - j\frac{\omega_o M^2 V_{\text{in}}}{R_{\text{ac}} L_{\text{in}}} \tag{12}$$

$$V_s = j\omega M I_p - j\omega L_s I_s = \frac{M V_{\text{in}}}{L_{\text{in}}} - j\frac{\omega_o L_s M V_{\text{in}}}{R_{\text{ac}} L_{\text{in}}} \tag{13}$$

$$V_{o,\text{ac}} = I_{o,\text{ac}} R_{\text{ac}} = \frac{M V_{\text{in}}}{L_{\text{in}}} \tag{14}$$

$$V_{Cs} = \frac{1}{j\omega C_s} I_s = -j\frac{\omega_o L_s M V_{\text{in}}}{R_{\text{ac}} L_{\text{in}}}. \tag{15}$$

As shown in Table I, the range of V_{batt} is from 240 to 410 V. In consideration of the boosting ratio of the BM converter under the lowest coupling coefficient condition ($k = 0.062$), V_o is designed as 165 V, and with this boosting ratio, V_o reaches to 510 V at the highest *k* condition ($k = 0.2$). However, a power semiconductor device with 650 V voltage rating is widely used for the secondary-side power circuit, the voltage stress due to the malfunction may cause the damage to the power semiconductor devices. Thus, phase-shift control for a full-bridge inverter is needed and V_o is limited to 450 V. A detailed explanation of the phase-shift control will be delivered in Section IV-A. Fig. 6(a) shows the parameter variation where L_p is set to $400\,\mu$H while L_s is changed from 100 to 300 μH by steps of $10\,\mu$H using (2)–(5). Fig. 6(b) and (c) illustrates the voltage and current stresses of the resonant network using (6)–(15). Considering the parameters and stresses, a design point is selected and presented in Fig. 6, and Table III shows the designed parameters of the

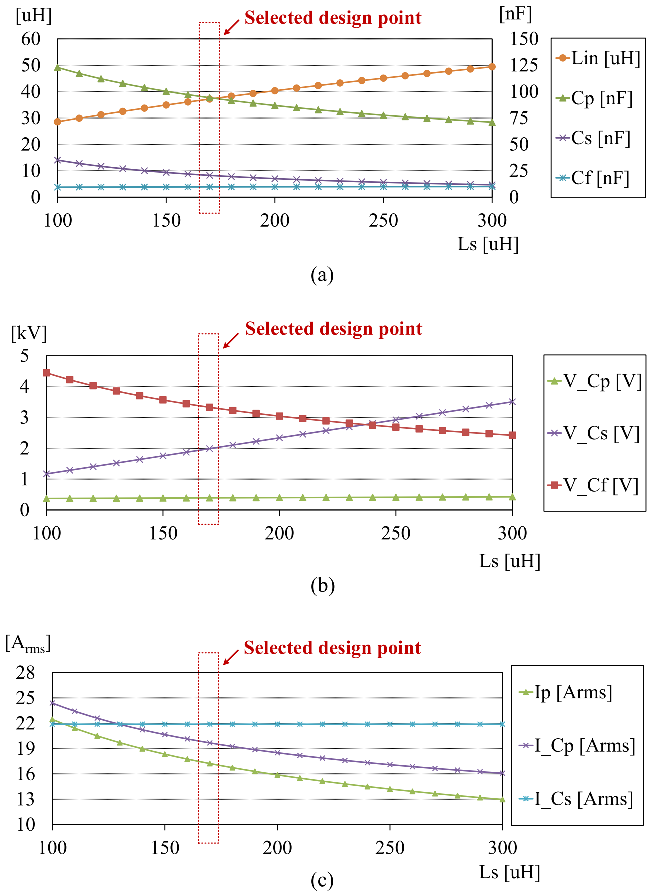

Fig. 6. Parameter and stress variations of the resonant network according to the L_s variation. ($L_p = 400\,\mu$H). (a) Parameter variation. (b) Voltage stresses of the resonant network. (c) Current stresses of the resonant network.

resonant network. The target P_o is set to 3350 W to deliver 3300 W to the load, considering the efficiency of the BM converter.

IV. CONTROL ALGORITHM OF THE PROPOSED SYSTEM

A. Proposed ZPA Tracking and Phase-Shift Control

In order to achieve high efficiency by reducing the turn-ON losses of the power semiconductors, zero-voltage switching (ZVS) is generally adopted for the PCS. Likewise, in the IPT system, for the purpose of reducing the voltage–ampere (VA) rating and increasing system efficiency, the ZPA operation, which is theoretically an in-phase operation, is preferred. However, because the proposed design method is based on the FHA, the derived ZPA frequency is the frequency at which the fundamental components of V_{in} and I_{in} are in phase, not the actually applied square-wave voltage and current with harmonics. Further, so as to minimize the effect of the dead time and harmonic component, ZPA tracking control is proposed. The previous research on ZPA tracking control needs to sense both V_{in} and I_{in} for phase detection and needs additional circuit to operate at ZPA or ZVS region [33]. However, the proposed control algorithm requires only I_{in} sensing circuit. By adjusting the operating frequency, the ZVS operation nearby ZPA frequency is possible, and this results in reducing reactive power and switching losses. Figs. 7 and 8 illustrate the I_{in} current sensing point of the proposed control and the block diagram of the ZPA tracking control algorithm.

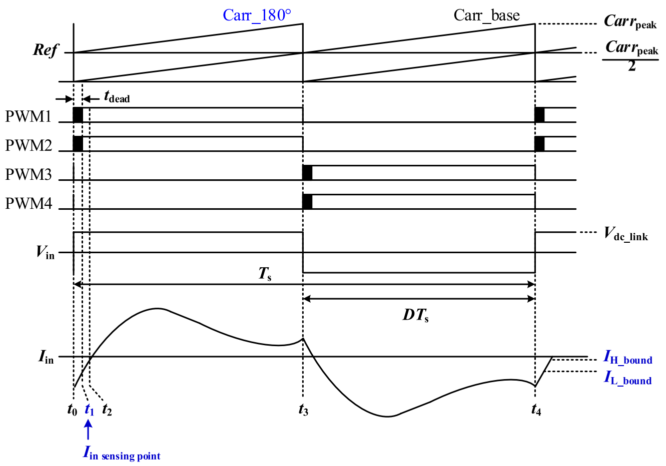

Fig. 7. Input current sensing point of the ZPA tracking control.

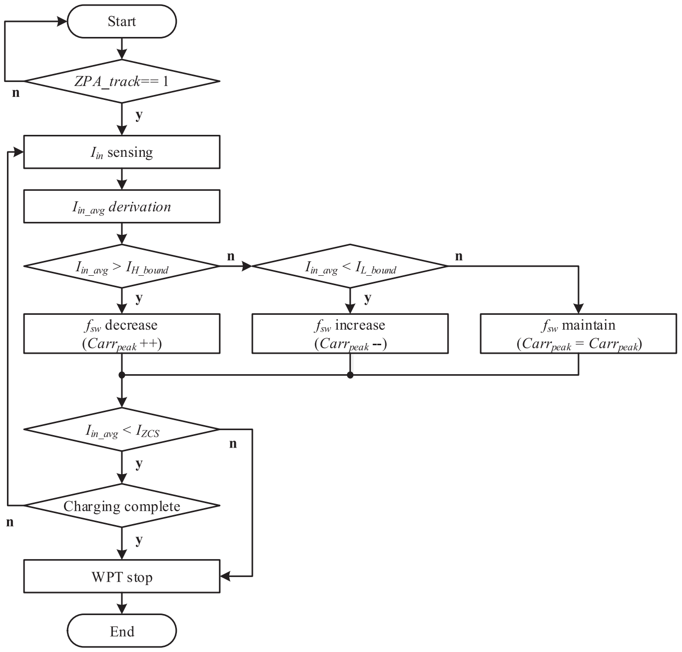

Fig. 8. Block diagram of the proposed ZPA tracking control algorithm.

The ZPA tracking control algorithm starts by sensing I_{in}. I_{in} is sensed at every interrupt period of the pulsewidth modulation controller, and the sensing point is set to t_1, which is the end of the dead time t_{dead}. When determining whether the frequency is increased or decreased by using the sensed I_{in} at every control period, the response time of the control will be faster, but the accuracy of the control is lowered if the sensing error occurs due to the external noise. Thus, using the moving average method, $I_{\text{in\_avg}}$ is derived by averaging the I_{in} values of the recent eight cycles. Since the phase of the *LCCL*-S topology is capacitive when the switching frequency $f > f_{\text{ZPA}}$ and inductive when $f < f_{\text{ZPA}}$ in the range of f_{sw}, the switching frequency is controlled to locate $I_{\text{in\_avg}}$ between $I_{L\text{\_bound}}$ and $I_{H\text{\_bound}}$. Ideally, the

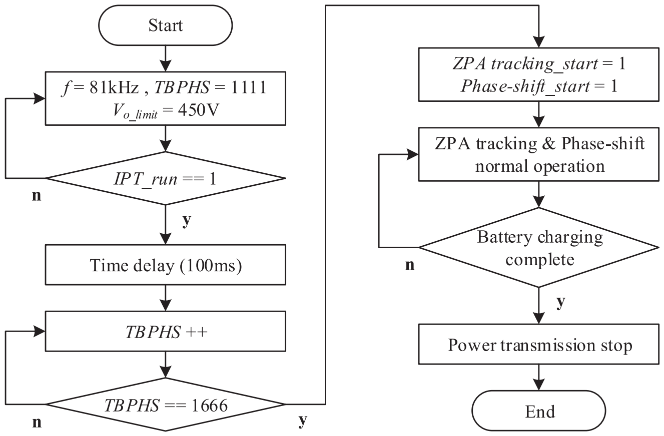

Fig. 9. Flowchart of the IPT converter control.

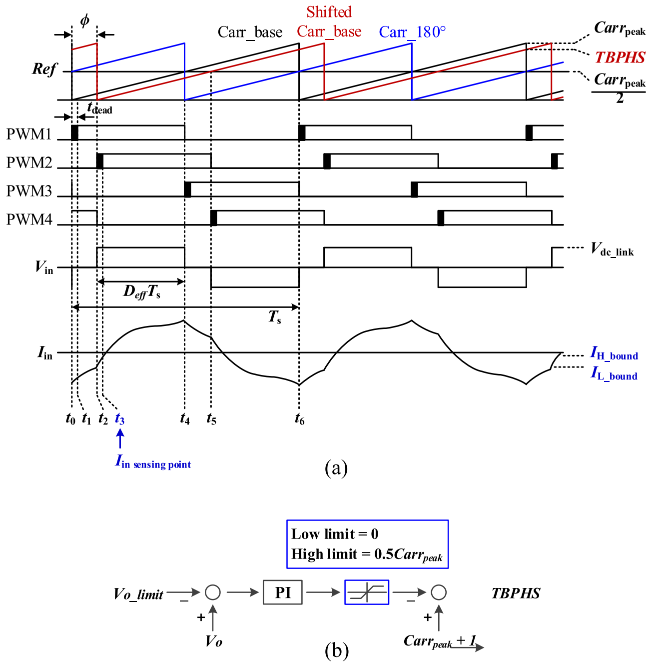

(a)

(b)

Fig. 10. Schematic of the proposed ZPA tracking and phase-shift control at V_o limiting operation. (Carr_peak 1765 ≒ 85 kHz). (a) Timing chart of the proposed ZPA tracking and phase-shift control at V_o limiting condition. (b) Control block of the V_o limiting phase-shift control.

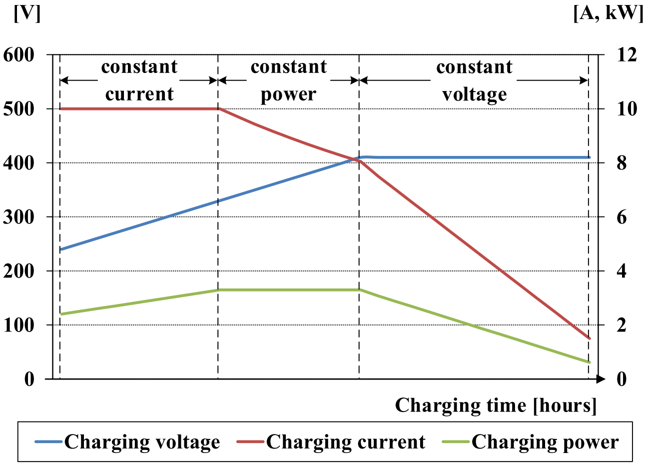

Fig. 11. Battery charging profile for the IPT system.

value of I_{H_bound} should be zero, and I_{L_bound} should be close to zero to operate at f_ZPA. However, since the switching frequency is determined by the quantized carrier of the digital controller, the switching frequency cannot be linearly controlled according to the carrier value [30]. Thus, the implementable maximum value of I_{L_bound} should be identified and the margin is necessary for I_{H_bound} to avoid hard switching of the switches. In order to protect the switching failure caused by the zero-current switching (ZCS) operation, I_ZCS is set, and if $I_{\text{in\_avg}}$ is larger than I_ZCS, ZCS flag is set. If the ZCS flag is still set after three attempts of trial, the WPT between is compulsorily terminated. In consideration of the aforementioned issues, the following values are determined: $I_{H\_\text{bound}} = -0.3$ A, $I_{L\_\text{bound}} = -1.3$ A, and $I_\text{ZCS} = 1$ A.

As mentioned in the Section III, V_o increases as k increases proportionally. Therefore, in order to correspond the V_o increment caused by high k, phase-shift control is applied to the IPT converter to regulate V_in. Considering the upper voltage limit of the BM converter's power semiconductors, the limitation value of the output voltage V_{o_limit} is set to 450 V. Figs. 9 and 10 illustrate the flowchart of the IPT converter and the schematic of the ZPA tracking and phase-shift control for V_o limiting operation. During the initial operation of the IPT converter, the switching frequency is set to 81 kHz to securely operate the system in the ZVS region. Further, for the purpose of preventing inrush due to C_p, the value of the time-base phase (TBPHS), which is the magnitude of the Shifted Carr_base where the magnitude of the Carr_base is zero, is configured to 1111 to set the effective duty D_eff to 0.1. If the operation of the IPT converter is enabled, the TBPHS is increased by step of one after a 100-ms time delay. By increasing the value of the TBPHS to 1666, D_eff also linearly increases to 0.4. Then, both ZPA tracking and phase-shift controls are enabled. If V_o is smaller than V_{o_limit}, only ZPA tracking control is applied, as shown in Fig. 7. In case it is higher, the V_o limiting phase-shift control is also applied. The control block of the V_o limiting phase-shift control is shown in Fig. 10(b).

B. BM Converter Control

The main function of the BM converter is to regulate the battery voltage while delivering the target power. Since the constant dc voltage is supplied from the IPT converter, the control of the BM converter is simple and its operation modes are determined by the relation of the input and output voltages of the BM converter. Figs. 11 and 12 show the CC-CP-CV battery charging profile and the flowchart of BM converter control to realize the battery charging profile. According to the battery charging profile, the reference values of the battery charging current $I_{\text{batt\_CC}}$ of the CC charging mode, the battery charging power $P_{\text{batt\_CP}}$ of the CP charging mode, and the battery charging voltage $V_{\text{batt\_CC}}$ of the CV charging mode are set to 10 A, 3.3 kW, and 410 V, respectively. At the beginning of the BM converter operation, as V_o reaches 160 V, CC mode is initiated, and when the power of the battery is greater than or equal to 3.3 kW, CP mode starts. The CP mode continues until the battery voltage reaches to 410 V,

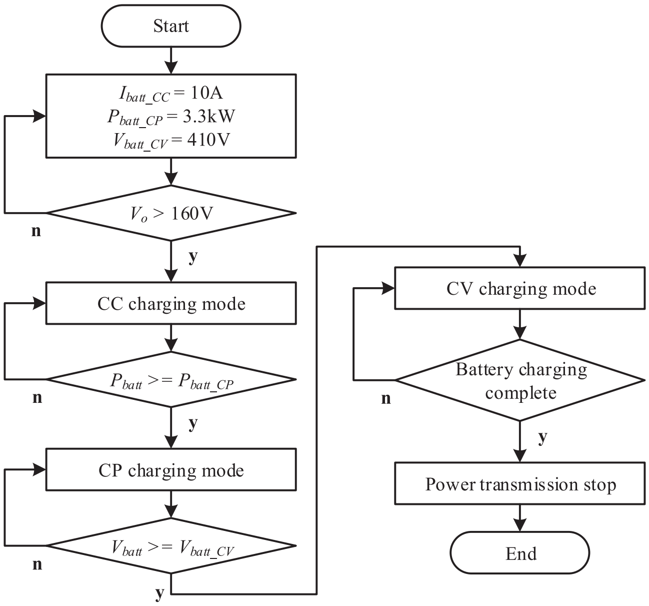

Fig. 12. Flowchart of the BM converter control.

and the during the CV mode, the battery voltage maintains a constant value of as 410 V by the time the battery charging is completed.

V. VERIFICATION

In order to verify the validity of the design and test, the performance of the proposed system, test bed, PCS, and magnetic power pads are manufactured, as shown in Fig. 13. The PCS is composed of a PFC converter, an IPT converter, and an BM converter, and the resonant capacitors are selected based on the numerical analysis and the magnetic power pads are made in reference to the SAE J2954. Figs. 14 and 15 illustrate the experimental waveforms of the PFC converter and IPT converter, respectively.

The performance of the PFC converter is evaluated under following conditions:

1) grid voltage: 220 V_{rms};
2) grid frequency: 60 Hz;
3) switching frequency: 60 kHz; and
4) output voltage: 380 V.

The load is implemented using an electrical load. As shown in Fig. 14(a), a phase current I_{La}, input current I_{grid}, and V_{dc_link} are well regulated. Fig. 14(b) depicts the load variation test from 400 W to 4 kW, and shows that the PFC converter is properly controlled as the load increases. The efficiency of the PFC converter is over 97% from 400 W and the power factor is higher than 0.99 over 25% of the load.

Fig. 15(a) and (b) illustrates the experimental waveforms of the IPT converter at $k = 0.062$ and Fig. 15(c) and (d) shows the experimental waveforms of the IPT converter at $k = 0.202$ where the output powers of the IPT converter P_o are 400 W and 3.4 kW, respectively. In Fig. 15(a) and (b), V_o is approximately 165 V and only ZPA tracking control is applied. Besides, in Fig. 15(c) and (d), V_o is limited to 450 V by V_o limiting phase-shift control and ZPA tracking control is also applied. Fig. 16 illustrates the steady-state waveforms of the BM converter at the beginning of the CC mode and the CV mode under various V_o and V_{batt} conditions. The switching frequency of the BM converter is set to 50 kHz.

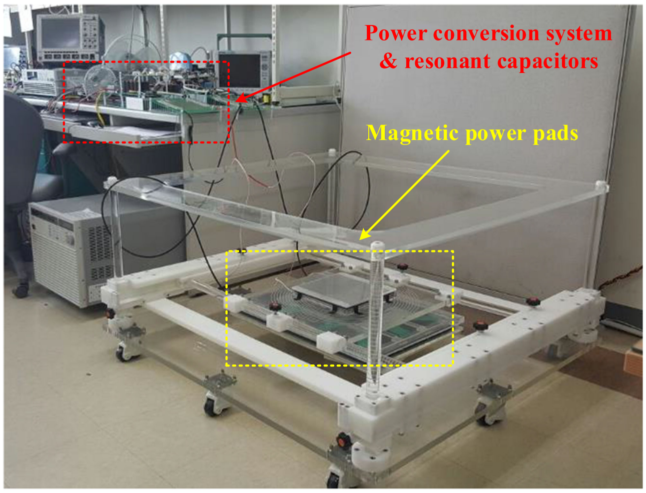

(a)

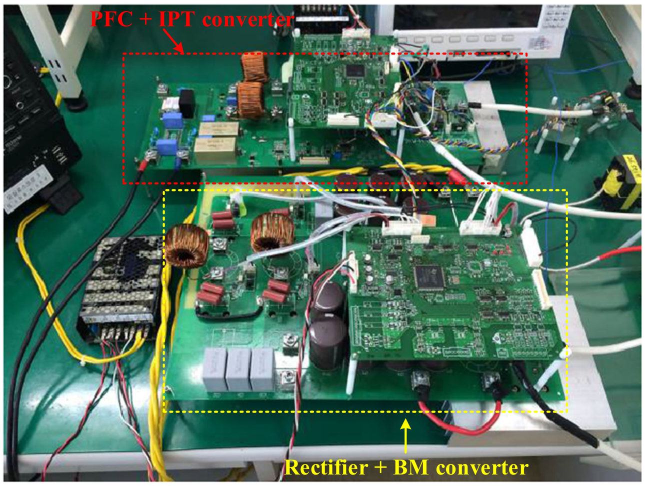

(b)

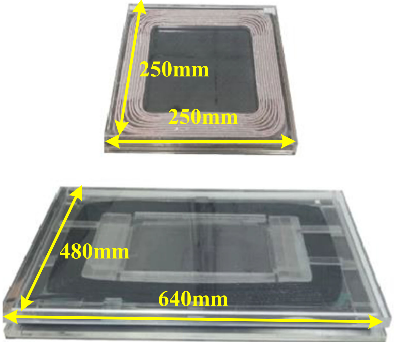

(c)

Fig. 13. Laboratory prototype of the proposed IPT system. (a) Test bed. (b) Power conversion system. (c) Manufactured magnetic power pads.

The BM converters in Fig. 16(a), (b), and (d) are operated by boost mode, whereas the ones in Fig. 16(c), (e), and (f) are

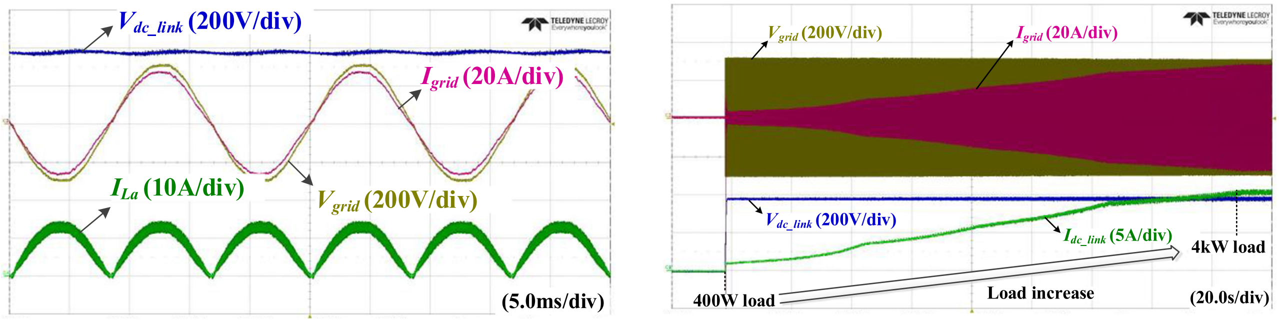

(a) (b)

Fig. 14. Experimental waveforms of the PFC converter. (a) Steady-state operation waveform of the PFC converter at 4-kW input. (b) Load variation results of the PFC converter from 400-W to 4-kW input.

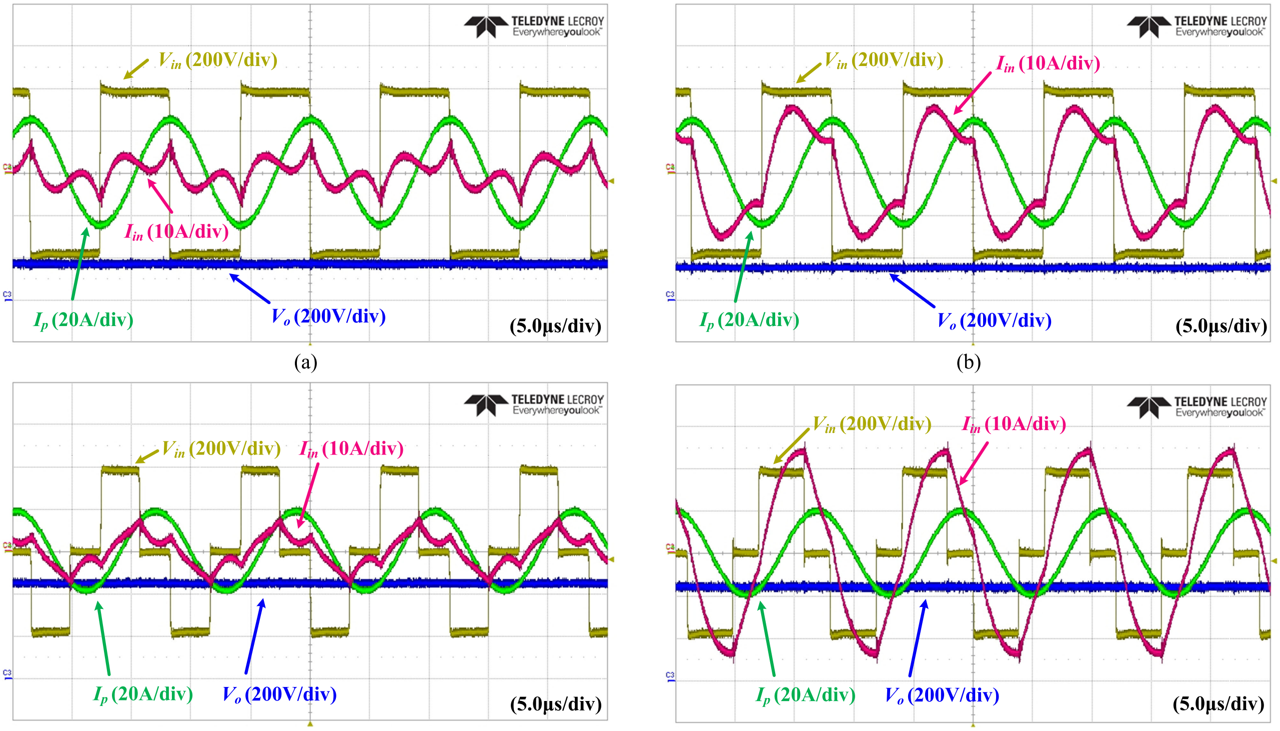

(a) (b)

(c) (d)

Fig. 15. Experimental waveforms of the IPT converter. (a) $k = 0.062$, $P_{o,\mathrm{ac}} = 400$ W, and $f_{\mathrm{sw}} = 85.04$ kHz. (b) $k = 0.062$, $P_{o,\mathrm{ac}} = 3400$ W, and $f_{\mathrm{sw}} = 84.46$ kHz. (c) $k = 0.202$, $P_{o,\mathrm{ac}} = 400$ W, and $f_{\mathrm{sw}} = 85.35$ kHz. (d) $k = 0.202$, $P_{o,\mathrm{ac}} = 3400$ W, and $f_{\mathrm{sw}} = 83.26$ kHz.

operated by buck mode. Regardless of V_o and V_{batt}, the phase current $I_{L1 \text{ or } L2}$, battery voltage V_{batt}, and battery current I_{batt} are well regulated. In order to verify the validity of the BM converter control, an electrical load is used to emulate battery load and Fig. 17 shows the CC-CP-CV control waveforms of the BM converter according to V_o.

According to the battery profile, the system is operated as boost mode in Fig. 17(a) and is operated as buck mode in Fig. 17(c). In case V_o is 300 V, the operation mode is moved from the boost to buck mode as the battery voltage increases during the CC mode. Although this operational transition occurs, the BM converter stably operates and it is presented in Fig. 17(b). Figs. 18 and 19 show the waveforms of the integrated IPT system.

As shown in Fig. 18, the initial operation of the integrated system at different *k* conditions performs well. In order to verify the CC-CP-CV charging control of the integrated system, the electrical load is used to emulate a battery load. During the CC mode, the current is set to 10 A until P_{batt} reaches to 3.3 kW, and during the CP mode, P_{batt} is maintained at 3.3 kW until V_{batt} reaches 410 V. After entering the CV mode, V_{batt} is kept at 410 V until the battery is fully charged. The experimental waveforms of the integrated IPT system applying the battery profile of Fig. 10 is shown in Fig. 19 and efficiency curve is shown in Fig. 20. Fig. 21 shows the efficiency of the proposed integrated IPT system according to *k* and load variation. Through the experimental results, a stable operation of each stage is iden-

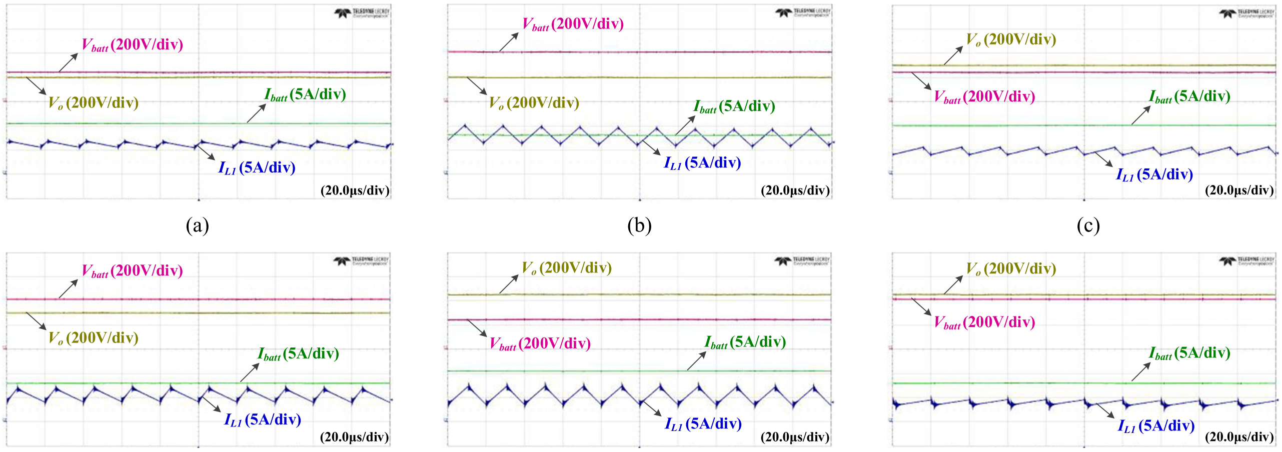

(a) (b) (c)

(d) (e) (f)

Fig. 16. Experimental waveforms of the BM converter under various input and output conditions. (a) $V_o = 200$ V, $V_{\mathrm{batt}} = 240$ V, and $P_{\mathrm{batt}} = 2.4$ kW. (b) $V_o = 200$ V, $V_{\mathrm{batt}} = 410$ V, and $P_{\mathrm{batt}} = 3.3$ kW. (c) $V_o = 300$ V, $V_{\mathrm{batt}} = 240$ V, and $P_{\mathrm{batt}} = 2.4$ kW. (d) $V_o = 300$ V, $V_{\mathrm{batt}} = 410$ V, and $P_{\mathrm{batt}} = 3.3$ kW. (e) $V_o = 450$ V, $V_{\mathrm{batt}} = 240$ V, and $P_{\mathrm{batt}} = 2.4$ kW. (f) $V_o = 450$ V, $V_{\mathrm{batt}} = 410$ V, and $P_{\mathrm{batt}} = 3.3$ kW.

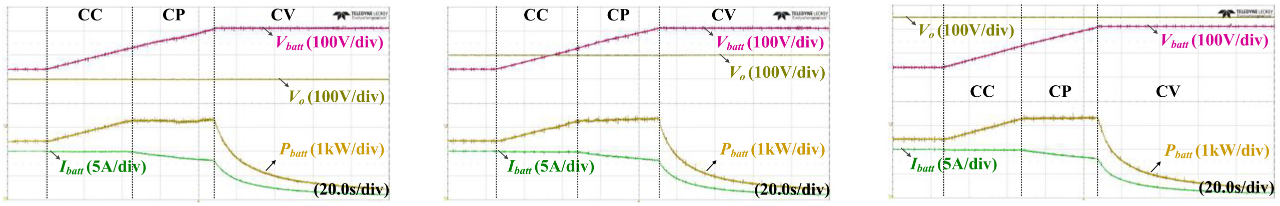

(a) (b) (c)

Fig. 17. CC-CP-CV control waveforms of the BM converter according to V_o. (a) $V_o = 200$ V. (b) $V_o = 300$ V. (c) $V_o = 450$ V.

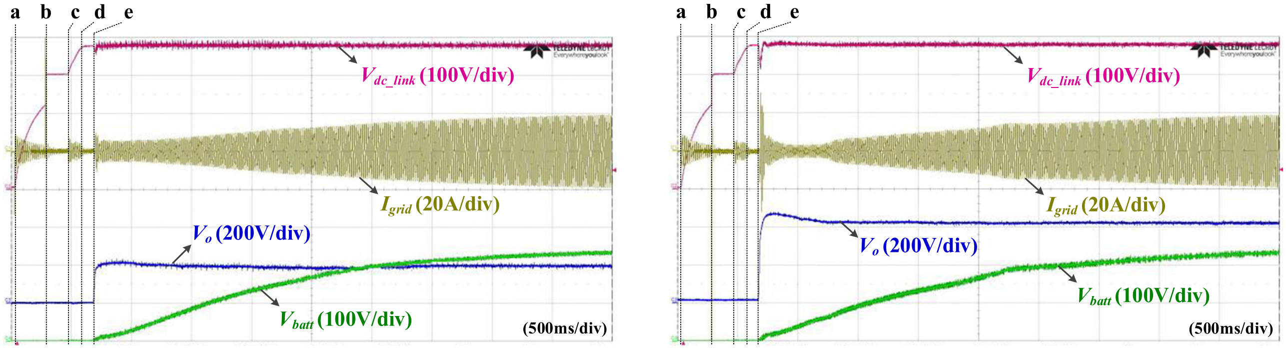

(a) (b)

Fig. 18. Initial operation waveforms of the integrated IPT system. (Point a: ac grid connection. Point b: precharging relay turn-ON. Point c: PFC converter soft start. Point d: IPT converter enable. Point e: beginning of the IPT converter operation ($V_o > 160$ V $\rightarrow$ starts of the BM converter operation)). (a) $k = 0.062$. (b) $k = 0.202$.

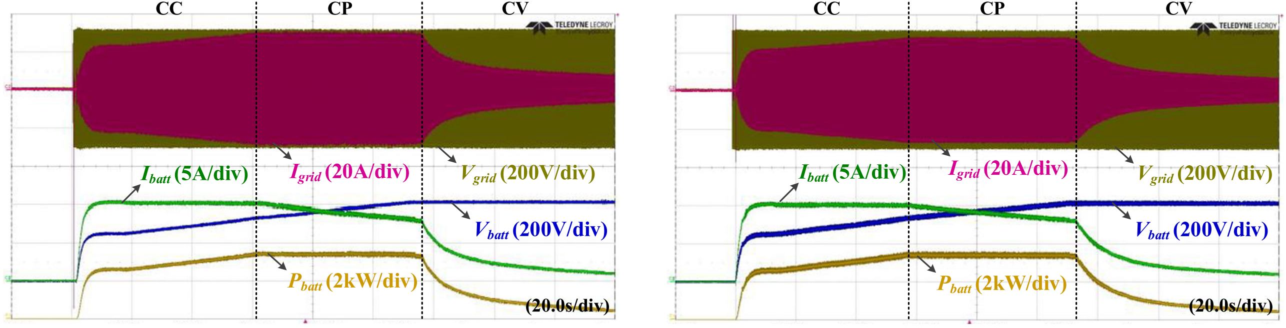

(a) (b)

Fig. 19. CC-CP-CV control of the integrated IPT system. (a) $k = 0.062$. (b) $k = 0.202$.

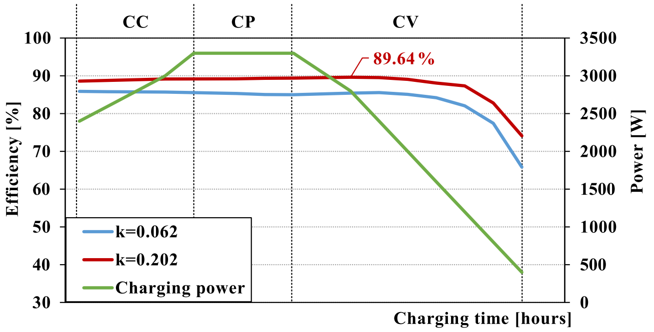

Fig. 20. Efficiency curve according to the battery profile.

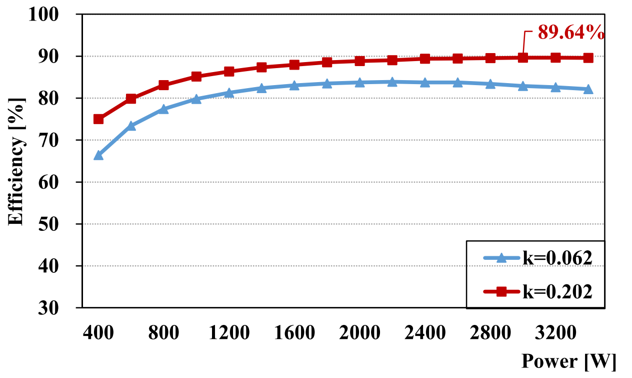

Fig. 21. Efficiency of the proposed integrated IPT system according to the k and load variation.

tified and the highest system efficiency is measured as 89.64% at 2.9 kW and $k = 0.202$.

VI. CONCLUSION

In this paper, a design and control scheme of the IPT system for EVs considering wide variations of the output voltage and coupling coefficient are proposed. The PCS and magnetic power pads of the proposed system are designed and manufactured in consideration of the SAE J2954. Among various kinds of resonant networks, *LCCL*-S topology is selected as the resonant network of the proposed system, and shows constant primary power pad current and output voltage characteristics, which is suitable for the design and control for EVs. The ZPA tracking control and V_o limiting phase-shift control for a IPT converter are also proposed. By adopting a BM converter at the final stage, the design and the control of the IPT converter is simplified and also the CC-CP-CV battery charging profile can be easily implemented. The initial and steady-state operations of each stage and integrated system are verified, and it is shown that the highest system efficiency is 89.64% at 2.9 kW, where the coupling coefficient is 0.202.

REFERENCES

[1] H. Takanashi, Y. Sato, Y. Kaneko, S. Abe, and T. Yasuda, "A large air gap 3 kW wireless power transfer system for electric vehicles," in *Proc. IEEE Energy Convers. Congr. Expo*, Raleigh, NC, USA, 2012, pp. 269–274.

[2] M. Kim, D.g-M. Joo, D.-G. Woo, and B. K. Lee, "Design and control of inductive power transfer system for electric vehicles considering wide variation of output voltage and coupling coefficient," in *Proc. IEEE Appl. Power Electron. Conf. Expo.*, Tampa, FL, USA, 2017, pp. 3648–3653.

[3] K. W. E. Cheng, B. P. Divakar, H. Wu, K. Ding, and H. F. Ho, "Battery-Management system (BMS) and SOC Development for electrical vehicles," *IEEE Trans. Veh. Technol.*, vol. 60, no. 1, pp. 76–88, Jan. 2011.

[4] C.-S. Wang, G. A. Covic, and O. H. Stielau, "Investigating an LCL load resonant inverter for inductive power transfer applications," *IEEE Trans. Power Electron.*, vol. 19, no. 4, pp. 995–1002, Jul. 2004.

[5] C.-S. Wang, O. H. Stielau, and G. A. Covic, "Design considerations for a contactless electric vehicle battery charger," *IEEE Trans. Ind. Electron.*, vol. 52, no. 5, pp. 1308–1314, Oct. 2005.

[6] R. Bosshard, J. W. Kolar, J. W. Mühlethaler, I. Stevanovic, B. Wunsch, and F. Canales, "Modeling and η-α-Pareto optimization of inductive power transfer coils for electric vehicles," *IEEE J. Emerg. Sel. Topics Power Electron.*, vol. 3, no. 1. pp. 50–64, Mar. 2015.

[7] X. Qu, Y. Jing, H. Han, S.-C. Wong, and C. K. Tse, "Higher order compensation for Inductive-Power-Transfer converters with Constant-Voltage or Constant-Current output combating transformer parameter constraints," *IEEE Trans. Power Electron.*, vol. 32, no. 1, pp. 394–408, Jan. 2017.

[8] Y. Wang, Y. Yao, X. Liu, D. Xu, and L. Cai, "An LC/S compensation topology and coil design technique for wireless power transfer," *IEEE Trans. Power. Electron.*, vol. 33, no. 3, pp. 2007–2025, Mar. 2018.

[9] K. Song, Z. Li, D. Zhijiang, G. Wei, and C. Zhu, "Design for constant output voltage and current controllability of primary side controlled wireless power transfer system," in *Proc. IEEE PELS Workshop Emerg. Technol. Wireless Power Trans.*, Chongqing, China, 2017, pp. 1–6.

[10] X. del Toro García, J. Vázquez, and P. Roncero-Sánchez, "Design, implementation issues and performance of an inductive power transfer system for electric vehicle chargers with series–series compensation," *IET Power Electron.*, vol. 8, no. 10, pp. 1920–1930, Oct. 2015.

[11] C.-Y. Huang, J. E. James, and G. A. Covic, "Design considerations for variable coupling lumped coil systems," *IEEE Trans. Power. Electron.*, vol. 30, no. 2, pp. 680–689, Feb. 2015.

[12] T. Kan, T.-D. Nguyen, J. C. White, R. K. Malhan, and C. C. Mi, "A new integration method for an electric vehicle wireless charging system using LCC compensation Topology: Analysis and design," *IEEE Trans. Power. Electron.*, vol. 32, no. 2, pp. 1638–1650, Feb. 2017.

[13] H. Feng, T. Cai, S. Duan, J. Zhao, X. Zhang, and C. Chen, "An LCC-Compensated resonant converter optimized for robust reaction to large coupling variation in dynamic wireless power transfer," *IEEE Trans. Ind. Electron.*, vol. 63, no. 10, pp. 6591–6601, Oct. 2016.

[14] G. Guidi and J. A. Suul, "Minimizing converter requirements of inductive power transfer systems with constant voltage load and variable coupling conditions," *IEEE Trans. Ind. Electron.*, vol. 63, no. 11, pp. 6835–6844, Nov. 2016.

[15] J. Hou, Q. Chen, S.-C. Wong, C. K. Tse, and X. Ruan, "Analysis and control of Series/Series-Parallel compensated resonant converter for contactless power transfer," *IEEE J. Emerg. Sel. Topics Power Electron.*, vol. 3, no. 1. pp. 124–136, Mar. 2015.

[16] J. Hou, Q. Chen, X. Ren, X. Ruan, S.-C. Wong, and C. K. Tse, "Precise characteristics analysis of series/series-parallel compensated contactless resonant converter," *IEEE J. Emerg. Sel. Topics Power Electron.*, vol. 3, no. 1. pp. 101–109, Mar. 2015.

[17] H. H. Wu, A. Gilchrist, K. D. Sealy, and D. Bronson, "A high efficiency 5kW inductive charger for EVs using dual side control," *IEEE Trans. Ind. Informat.*, vol. 8, no. 3, pp. 585–595, Aug. 2012.

[18] X. Qu, H. Han, S.-C. Wong, C. K. Tse, and W. Chen, "Hybrid IPT topologies with constant current or constant voltage output for battery charging applications," *IEEE Trans. Power Electron.*, vol. 30, no. 11, pp. 6329–6337, Nov. 2015.

[19] SAE International, "Wireless power transfer for light-duty plug-in/electric vehicles and alignment methodology," 2017. [Online]. Available: http://standards.sae.org/wip/j2954/

[20] V. B. Vu, D. H. Tran, and W. Choi, "Implementation of the constant current and constant voltage charge of inductive power transfer systems with the Double-Sided LCC compensation topology for electric vehicle battery charge applications," *IEEE Trans. Power Electron.*, to be published. [Online]. Available: https://ieeexplore.ieee.org/stamp/stamp.jsp?tp=&arnumber=8085158

[21] D. H. Tran, V. B. Vu, and W. Choi, "Design of a High-Efficiency wireless power transfer system with intermediate coils for the on-board chargers of electric vehicles," *IEEE Trans. Power Electron.*, vol. 33, no. 1, pp. 175–187, Jan. 2018.

[22] *IEEE Recommended Practice and Requirements for Harmonic Control in Electric Power Systems*, IEEE Standard 519-2014, 2014.

[23] C.-Y. Huang, "Design of IPT EV battery charging systems for variable coupling applications," Ph.D. dissertation, Dept. Elect. Eng., Auckland Univ., Auckland, New Zealand, 2011.

[24] M. Budhia, G. A. Covic, and J. T. Boys, "Design and optimization of circular magnetic structures for lumped inductive power transfer systems," *IEEE Trans. Power Electron.*, vol. 26, no. 11, pp. 3096–3108, Nov. 2011.

[25] M. Budhia, G. A. Covic, and C.-Y. Huang, "Development of a Single-Sided flux magnetic coupler for electric vehicle IPT charging systems," *IEEE Trans. Ind. Electron.*, vol. 60, no. 1, pp. 318–328, Jan. 2013.

[26] M. Budhia, G. A. Covic, J. T. Boys, and C.-Y. Huang, "Development and evaluation of single sided flux couplers for contactless electric vehicle charging," in *Proc. IEEE Energy Convers. Congr. Expo.*, Phoenix, AZ, USA, 2011, pp. 614–621.

[27] A. Zaheer, D. Kacprzak, and G. A. Covic, "A bipolar receiver pad in a lumped IPT system for electric vehicle charging applications," in *Proc. IEEE Energy Convers. Congr. Expo.*, Raleigh, NC, USA, 2012, pp. 283–290.

[28] S. Wang and D. G. Dorrell, "Loss analysis of circular wireless EV charging coupler," *IEEE Trans. Mag.*, vol. 50, no. 11, Nov. 2014, Art. no. 8402104.

[29] M. Kim, J. Byeon, J.-W. Lee, and B. K. Lee, "Performance analysis of magnetic power pads for inductive power transfer systems with ferrite structure variation," *J. Elect. Eng. Technol.*, vol. 12, no. 3, pp. 1211–1218, May. 2017.

[30] D.-G. Woo, "Optimal design and control strategy of inductive power transfer charging system for electric vehicles," Ph.D. dissertation, Dept. Elect. Eng., Sungkyunkwan Univ., Suwon, South Korea, 2015.

[31] C.-S. Wang, G. A. Covic, and O. H. Stielau, "Power transfer capability and bifurcation phenomena of loosely coupled inductive power transfer systems," *IEEE Trans. Ind. Electron.*, vol. 51, no. 1, pp. 148–157, Feb. 2004.

[32] R. L. Steigerwald, "A comparison of half-bridge resonant converter topologies," *IEEE Trans. Power Electron.*, vol. 3, no. 2, pp. 174–182, Apr. 1988.

[33] N. Liu and T. G. Habetler, "Design of a universal inductive charger for multiple electric vehicle models," *IEEE Trans. Power Electron.*, vol. 30, no. 11, pp. 6378–6390, Nov. 2015.

Minkook Kim (S'14) received the B.S. degree from Sungkyunkwan University, Suwon, South Korea, in 2012. Since 2012, he has been working toward the Masters/Ph.D. degree in electrical engineering with Sungkyunkwan University.

His research interest focuses on the inductive power transfer system for electric vehicles.

Dong-Myoung Joo (S'14) received the B.S., M.S., and Ph.D. degrees from Sungkyunkwan University, Suwon, South Korea, in 2011, 2013, and 2017, respectively, all in electrical engineering.

From 2015 to 2016, he was a Postdoctoral Researcher with Sungkyunkwan University. From 2018, he has been a Part-Time Lecturer in Shandong University of Technology, Beijing, China. His research interests include power conditioning system with inductive power transfer and WBG semiconductor devices for hybrid electric vehicles/electric vehicles.

Byoung Kuk Lee (S'97–M'02–SM'04) received the B.S. and the M.S. degrees from Hanyang University, Seoul, South Korea, in 1994 and 1996, respectively, and the Ph.D. degree from Texas A&M University, College Station, TX, USA, in 2001, all in electrical engineering.

From 2003 to 2005, he was a Senior Researcher with Power Electronics Group, Korea Electrotechnology Research Institute, Changwon, South Korea. In 2006, he joined the College of Information and Communication Engineering, Sungkyunkwan University, Suwon, South Korea. His research interests include on-board chargers and wireless power transfer chargers for electric vehicles, BMS algorithms, energy storage systems, hybrid renewable energy systems, dc distribution systems for home appliances, modeling and simulation, and power electronics.

Prof. Lee is currently a Guest Associate Editor for the IEEE TRANSACTIONS ON POWER ELECTRONICS and an Associate Editor for the IEEE TRANSACTIONS ON TRANSPORTATION ELECTRIFICATION. He was the Presenter for Professional Education Seminar with the topic of "On-Board Charger Technology for EVs and PHEVs" for the IEEE Applied Power Electronics Conference in 2014. He was the General Chair for the IEEE Vehicular Power and Propulsion Conference in 2012 and has been a member of IEC Conformity Assessment Board from 2016. He was the recipient of the Outstanding Scientists of the 21st Century from IBC and listed on 2008 Ed. of Who's Who in America and 2009 Ed. of Who's Who in the World.